7

Fast high resolution whole brain T_2^* weighted imaging using echo planar imaging at 7 Tesla

J.J.M. Zwanenburg
M.J. Versluis
P.R. Luijten
N. Petridou

NeuroImage 2011, 56(4): 1902-1907

ABSTRACT

Magnetic susceptibility based (T_2*-weighted) contrast in MRI at high magnetic field strength is of great value in research on brain structure and cortical architecture, but its use is hampered by the low signal-to-noise ratio (SNR) efficiency of the conventional spoiled gradient echo sequence (GRE) leading to long scan times even for a limited number of slices. In this work, we show that high resolution (0.5 mm isotropic) T_2*-weighted images of the whole brain can be obtained in 6 min by utilizing the high SNR efficiency of echo-planar imaging (EPI). A volumetric (3D) EPI protocol is presented and compared to conventional 3D GRE images acquired with the same resolution, amount of T_2*-weighting, and imaging duration. Spatial coverage in 3D EPI was increased by a factor of 4.5 compared to 3D GRE, while also the SNR was increased by a factor of 2. Image contrast for both magnitude and phase between gray and white matter was similar for both sequences, with enhanced conspicuity of anatomic details in the 3D EPI images due to the increased SNR. Even at 7 T, image blurring and distortion is limited if the EPI train length remains short (not longer than the T_2* of the imaged tissue). 3D EPI provides steps (speed, whole brain coverage, and high isotropic resolution) that are necessary to utilize the benefits of high field MRI in research that employs T_2*-weighted imaging.

INTRODUCTION

Magnetic resonance imaging (MRI) with susceptibility-based contrast at high magnetic field strength has allowed the visualization of human brain anatomy in vivo with exceptional detail. Variations in magnetic susceptibility of tissue (manifested as T_2^* and frequency variations) yield clear contrast between different anatomical structures in T_2^*-weighted magnitude images both in white matter (e.g. fiber bundles (1)) and gray matter (e.g. basal ganglia (2)). The phase of T_2^* weighted images is even more sensitive to magnetic susceptibility variations. Using the phase, it is possible to depict exquisite details of cortical structure and substructure, including the line of Gennari in the visual cortex (3–5). The magnetic susceptibility of tissue depends on the presence and arrangement of, amongst others, lipids, proteins and (non-heme) iron in the tissue (6, 7). T_2^*-weighted imaging at high field is, therefore, sensitive to the tissue composition at a cellular level, yielding a powerful tool to study normal and pathological tissue (8–11).

T_2^*-weighted imaging is conventionally performed using a spoiled gradient echo (GRE) sequence (12). At the high resolutions employed to image structural detail (<<1 mm3 voxel volume), however, imaging time is long, even for a limited number of slices (3). As a result, the imaging volume is typically limited since full brain coverage requires excessively long scan times of 1 h or more for a single acquisition. This hampers the practical use of T_2^*-weighted imaging for fundamental research of normal physiology or disease. Long imaging times are also problematic because they increase the possibility of subject motion during the scan duration resulting in blurring or unusable images (13). The long imaging times are due to the relatively low signal-to-noise ratio (SNR) efficiency of the spoiled GRE sequence. For sufficient T_2^* weighting, a long echo time (TE) is needed, which leads to 'dead' time in the sequence during which no signal is acquired.

In this work, we show that high resolution T_2^*-weighted images of the whole brain can be obtained in 6 min based on volumetric (3D) echo-planar imaging (EPI) by utilizing the high SNR efficiency of EPI (14). By using a multi-shot approach with short EPI train lengths, the common artifacts related to EPI (distortion and blurring) are limited, and images with a considerable gain in both SNR and coverage as compared to GRE imaging can be obtained within a given amount of scan time. The contrast in the phase and magnitude 3D EPI images and the distortion are compared with 3D GRE images, acquired with the same acquisition parameters in terms of resolution, amount of T_2^*-weighting, and imaging duration.

MATERIALS AND METHODS

Imaging was performed on 8 healthy subjects (4 male, 4 female, age 27 ± 4 years) who gave written informed consent, in accordance to the Institutional Review Board of the University Medical Center Utrecht. Images were acquired using a 7 T MRI system (Philips Healthcare, Cleveland, USA) with a 16 channel receive coil and a volume transmit coil (Nova Medical, Wilmington, MA). Maximum gradient strength and slew rate were 33 mT/m and 166 T/m/s, respectively. For all sequences 3rd order B_0 shimming was performed using an image based approach with an adapted version of the tool developed by (15). The amplitude of the RF transmit field (B_1) was measured with actual flip angle imaging in the pulsed steady state (16) in order to assess the spatial variations in the RF transmit field across the brain, using the following parameters: TR1/TR2/TE 25/125/2.5 ms, flip angle 50°, voxel size 3.8 × 3.7 × 4 mm^3, 20 slices, field of view 240 × 195 mm^2. For good T_2* contrast, the TE of the T_2*-weighted sequences was chosen to be equal to the average T_2* of white matter at 7 T: 27 ms (17), which is in between the (on average longer) T_2* of cortical gray matter and the (on average shorter) T_2* of the iron containing nuclei of the basal ganglia.

3D EPI protocol

A 3D T_2*-weighted protocol was set up with 0.5 mm isotropic resolution (125 nl voxel volume) and whole brain coverage, with a total scan duration of less than 6 min. Multi-shot 3D EPI was used with a conventional Cartesian interleaved *k*-space trajectory. During each EPI shot, the *y* gradient (left–right (LR) encoding) was stepped, for a given k_z (linearly increasing phase encoding step in the feet–head direction). The EPI factor was set to 13, leading to an EPI train length of 23 ms, below the average T_2* for gray and white matter (17). Fat-suppression was applied to avoid possible artifacts that may arise from a shifted fat signal in combination with sensitivity encoding (SENSE) with the small receive coils, which have a rapidly varying sensitivity at the location of the subcutaneous fat. For fat-suppression Spectral Presaturation Inversion Recovery (SPIR) was applied with a non-selective RF pulse of 110 ° flip angle, 679 Hz BW and a frequency offset of 1.1 kHz. The flip angle of the imaging sequence was set to a value which was 33% larger than the Ernst angle for gray matter given the TR (see Table 1). This choice was made to partly compensate for the fact that the actual B_1 as assessed from the B_1 maps was about 80% of the nominal value (20 μT) in the center of the brain, and even less elsewhere. The Ernst angle was computed using the T_1 value for cortical gray matter at 7T, T_1 = 2132 ms (18). The flip angle was optimized for gray matter (GM), as GM has a longer T_1 and thus less signal, relative to white

matter (WM). The imaging parameters are shown in Table 1.

Table 1: Imaging parameters.

	3D EPI	3D GRE	2D EPI	2D GRE
FOV (mm^2)	240 × 192	240 × 192	240 × 190	240 × 190
Matrix (AP × RL)	480 × 381	480 × 384	300 × 234	300 × 237
Resolution (mm2)	0.5 × 0.5	0.5 × 0.5	0.8 × 0.8	0.8 × 0.8
Slice thickness (mm)	0.5	0.5	2	2
Nr slices	300	66	1	1
Coverage (FH direction, mm)	150	33	2	2
Flip angle	19°	13°	15°	15°
TR/TE (ms)	70/27	32/27	70/27	70/27
BW readout direction (Hz/pixel)	677	203	997	1080
BW phase encoding direction (Hz/pixel)	41	–	57	–
EPI factor	13	–	13	–
Repetitions[a]	–	–	26	2
Slice-oversampling factor	1.28	1.28	–	–
k-space shutter (sampled fraction of k-space)	1.0	0.78	1.0	1.0
SENSE (LR)	2.3	2.3	1.0	1.0
Fat suppression	SPIR	None	SPIR	SPIR
Scan time (s)	350	354	33.3	33.9

FOV: field-of-view, AP: anterior–posterior, RL: left–right, FH: feet–head, TR: repetition time, TE: echo time, BW: bandwidth, SENSE: parallel imaging acceleration factor (sensitivity encoding), SPIR: spectral presaturation by inversion recovery. [a] Last repetition is performed without applying any RF or gradient pulses in order to measure the noise.

3D GRE protocol

As a reference for image quality, a GRE imaging protocol was set up with the same resolution, TE and scan duration as the EPI protocol (Table 1). The bandwidth was chosen to obtain optimal SNR for the GRE images, and was equivalent to that used for the combined time-of-flight/susceptibility weighted clinical imaging protocols in our hospital (19). Given the scan duration, coverage for the GRE protocol was maximized by choosing the shortest possible repetition time (TR), and adapting the flip angle accordingly. Fat suppression was omitted to further shorten the TR within the specific absorption rate (SAR) constraints. A vendor supplied elliptical shutter in *k*-space was

applied with GRE, which means that approximately 22% of the data in the edges with both high k_y and high k_z values were not sampled. Given the scan duration, this allows to further increase the coverage with a limited cost in resolution.

Quantitative comparison between 3D EPI and 3D GRE images

The 3D EPI and GRE images were reconstructed with image homogeneity correction, using the standard reconstruction software of the scanner. Both magnitude and phase images were stored. Phase images were high-pass filtered by subtracting a 2nd order polynomial fit from the phase data in order to remove large length-scale fields over the whole image. Varying fields toward the edge of the image were filtered by modeling these fields with dipole point sources parallel to the main field (B_0) and subtracting a least-squares fit from the phase data, as described in Wharton et al. (20) The 3D EPI images were compared to the GRE images to assess the image quality and contrast, for both magnitude and phase.

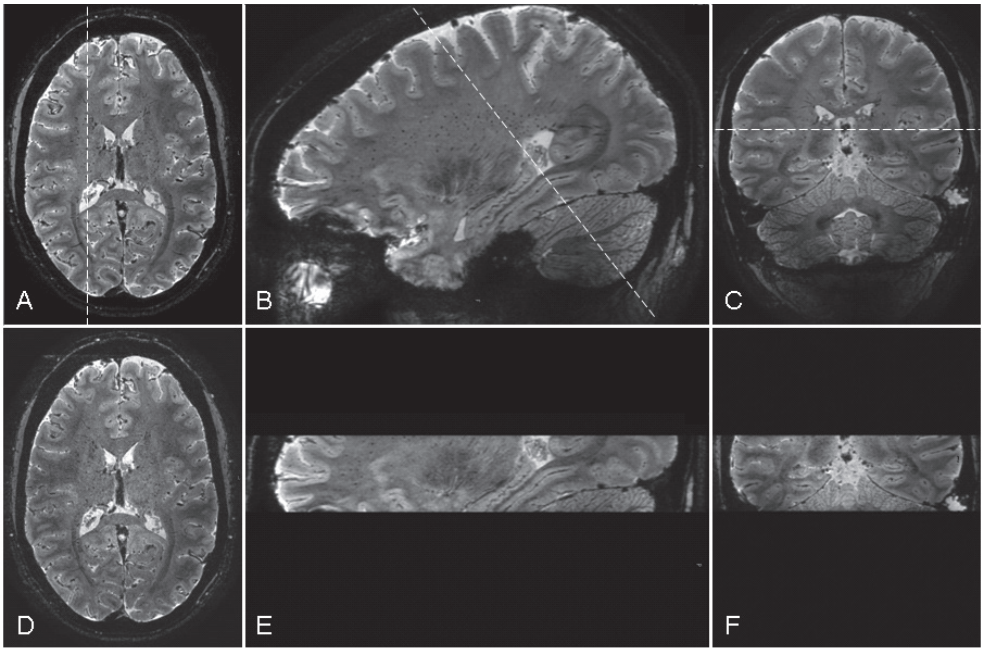

Figure 1: Magnitude images of the 3D EPI protocol
(A: transverse, B: sagittal, C: coronal orientation), showing the gain in coverage and SNR as compared to the 3D GRE imaging protocol (D, E and F). Note that the EPI and GRE images are acquired with the same scan duration and resolution. The dotted lines indicate the perpendicular cross-sections of the different orientations. Some blurring can be seen for the GM just above the nasal cavity in panel B.

The contrast between GM and WM in the two sequences was compared for regions of interest (ROIs) in three different regions (GM vs. WM): cingulate gyrus vs. corpus callosum, putamen vs. internal capsule, and GM vs. WM in the primary visual cortex. The contrast in the magnitude images was defined as the signal of GM divided by the signal of WM. This signal ratio was chosen, because the conventional measure of contrast, $SNR_{GM} - SNR_{WM}$ is directly affected by the overall difference in SNR between the two sequences. The contrast in the phase images was quantified as the frequency difference in Hz, which was obtained by dividing the phase in radians by 2π TE.

The distortion in the EPI images was assessed by overlaying the outer contour of the GM in the 3D GRE image over the corresponding 3D EPI image. To remove any contribution from head motion between the scans, the 3D GRE images were registered to the 3D EPI images with rigid body registration using the FSL software package (FSL 4.1, FMRIB's Software Library, Oxford (21). After registration, the maximum mismatch between the GRE contour and the EPI image was measured in the phase encoding (LR) direction for both the lowest and the highest slice in the GRE dataset.

To confirm that the EPI and GRE performance is equivalent if all imaging parameters are the same, we performed a 2D experiment where the only difference was the scan duration (due to the EPI factor). The imaging parameters are given in Table 1. The noise level was measured by repeating the data acquisition with the same receiver gain and bandwidth for data sampling, without applying any RF or gradient pulses. The EPI scan was repeated multiple times in dynamic mode, in order to obtain a steady state signal for correct comparison of the SNR level between EPI and GRE imaging. The 2D EPI and GRE images were used to measure the SNR in an ROI covering the complete brain. The noise level was quantified as the standard deviation in a corresponding ROI in the image with sampled noise.

RESULTS

The image quality was consistent for all volunteers for both the 3D EPI and the 3D GRE protocol. The remarkable improvements in both coverage and SNR that are obtained with the 3D EPI protocol are illustrated in Fig. 1. Note the clear depiction of the cerebellum, and the clear visualization of the hippocampus in the 3D EPI images. The contrast in both the magnitude and phase images between GM and WM was similar between 3D EPI and 3D GRE, as shown in Table 2. Fig. 2 and Fig. 3 illustrate the improved image SNR with 3D EPI, for sample areas in the basal ganglia and the visual cortex. The higher SNR in the 3D EPI magnitude images yields improved visualization of tissue

borders, for example between white matter and the putamen, hippocampus and substantia nigra (Fig. 2). Also the optic radiations are delineated more clearly as they fuse into the primary visual cortex (Fig. 3). In analogy to the magnitude images, the higher SNR obtained with 3D EPI yields clearer phase images, which allows enhanced visualization of subtle details such as the line of Gennari in the visual cortex (Fig. 3). Artifacts from incomplete phase unwrapping are similar between both protocols, e.g. posteriorly around the edges of the cortex (Fig. 2 and Fig. 3).

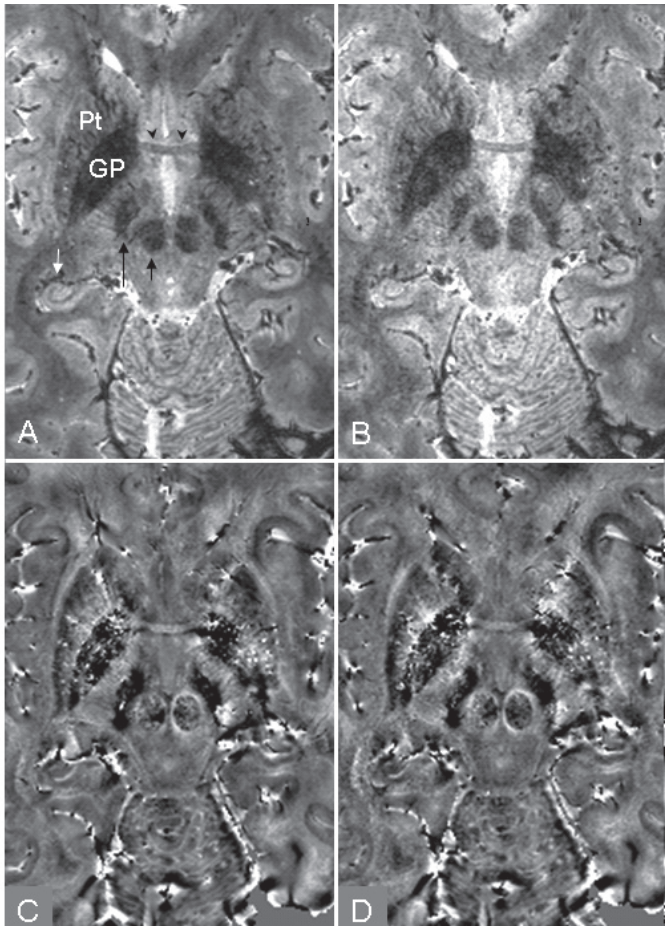

Figure 2: Detail of transverse 3D EPI vs. 3DGRE images.
Visible are many anatomical structures,including the putamen (Pt) and globus pallidus (GP) in the lentiform nucleus, the anteriorcommissure (black arrow heads), substantia nigra (long black arrow), the nucleus ruber (short black arrow) and the hippocampus (white arrow). Left: 3D EPI magnitude (A) and phase (C). Right: 3D GRE magnitude (B) and phase (D).

Maximum image distortions measured in the 3D EPI images, were 2.2 ± 0.5 mm and 1.1 ± 0.2 mm for the slice corresponding to the lowest and

highest slice in the 3D GRE volume, respectively. The maximum distortion was usually observed as a very localized distortion (as illustrated in Fig. 4). In many cases, particularly away from bone/air-tissue interfaces, the distortion (if present) was less than 0.5 mm (pixel size). An example of the distortion is given in Fig. 4. In the slices close to the skull base, the border between GM and WM appeared less sharp in the EPI images, as can be seen in the frontal area above the nasal cavities in Fig. 1.

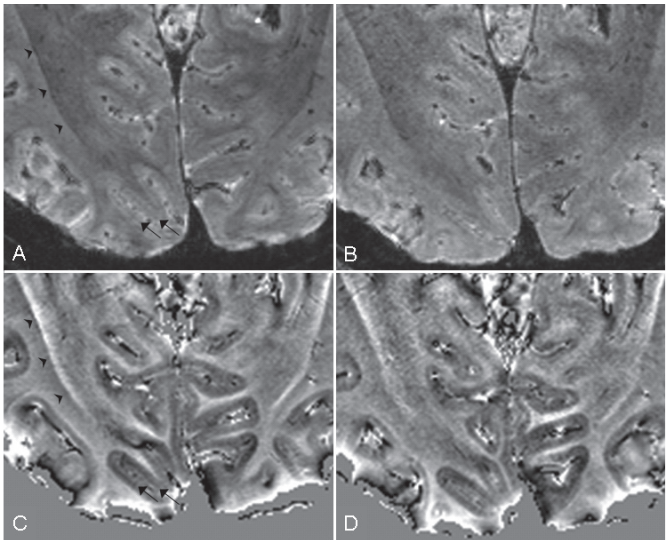

Figure 3: Detail of transverse 3D EPI vs. 3D GRE images, showing part of the visual cortex. Left: 3D EPI magnitude (A) and phase (C). Right: 3D GRE magnitude (B) and phase (D). The black arrows in the EPI phase image (C) indicate the line of Gennari, and the arrow heads point to the clear delineation of the optic radiations.

The 2D EPI images had similar SNR (15.8 ± 0.6) as the 2D GRE images (14.9 ± 0.5) (mean ± standard deviation across subjects, n = 8), despite the fact that they were acquired 13 times faster. Hence, the SNR efficiency of the 2D EPI protocol was approximately √ 13 larger than that of 2D GRE protocol, as expected.

DISCUSSION

The high SNR efficiency of EPI was used to develop a fast 3D T_2*-weighted anatomical imaging protocol, providing whole brain coverage with 0.5 mm isotropic resolution in less than 6 min. Given a fixed amount of scan time, the 3D EPI protocol yields more than a four-fold increase in coverage (150 mm vs. 33 mm for 3D GRE imaging), and also higher SNR. The higher SNR allows enhanced visualization of fine anatomical detail (Fig. 2 and Fig. 3), while the

isotropic resolution allows reformatting of the data in any desired orientation (Fig. 1).

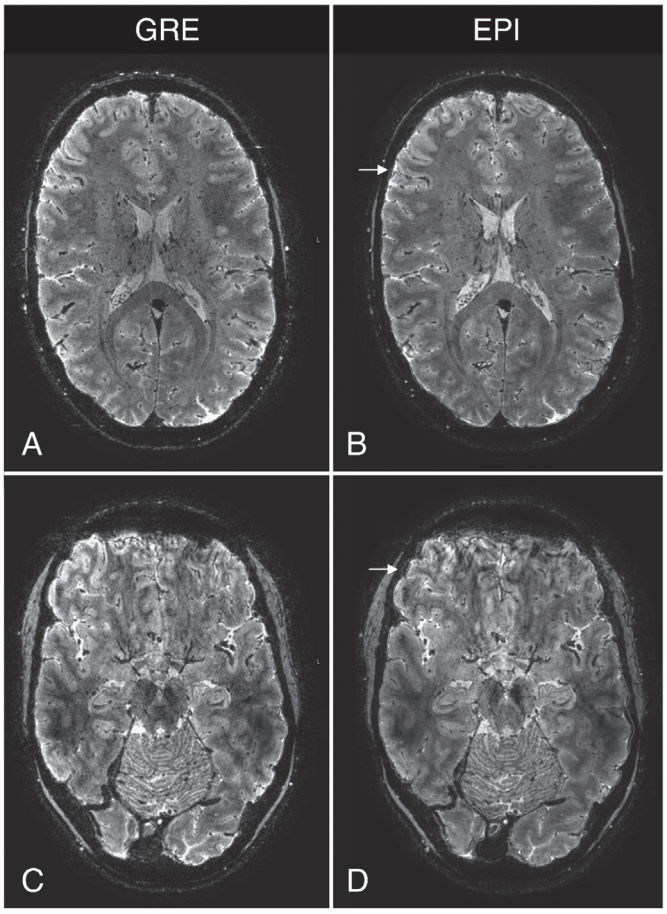

Figure 4: Amount of distiortions on GRE and EPI dataset.
Example data showing the highest and lowest slices of a 3D GRE data set (panels A and C, respectively) and the corresponding slices in the 3D EPI data set (panels B and D, respectively). The outer contours of the brain as drawn on the GRE images are superimposed on the EPI images to assess the amount of distortion. The arrows indicate the location of maximum distortion in the phase encoding direction (1.4mm for the highest slice, B, and 2.7 mm for the lowest slice, D).

To date, the high SNR efficiency of EPI is almost exclusively used for functional MRI (fMRI), to capture the dynamic signal changes associated with brain activity. Recently, it was shown that 3D EPI imaging is more efficient than multi-slice (2D) EPI, in the context of fMRI applications (22). The current results show that the high SNR efficiency of 3D EPI is also valuable for application in structural imaging, an application for which the use of EPI seems to be underappreciated.

Table 2. Contrast between GM and WM for both 3D EPI and 3D GRE images.

	3D EPI magnitude	3D GRE magnitude	3D EPI phase (Hz)	3D GRE phase (Hz)
CG vs.CC	1.7 ± 0.2	1.7 ± 0.2	− 0.3 ± 0.7	− 0.2 ± 0.5
Pt vs. IC	0.8 ± 0.1	0.8 ± 0.1	− 2.6 ± 0.4	− 2.4 ± 0.5
GM_{vc} vs. WM_{vc}	1.2 ± 0.2	1.1 ± 0.1	− 3.4 ± 1.0	− 3.5 ± 1.2

CG: cingulated gyrus, CC: corpus callosum, Pt: putamen, IC: internal capsule, GM_{vc}/WM_{vc}: gray matter/white matter of visual cortex. For magnitude: ratio of gray matter signal over white matter signal, for phase: difference in phase, expressed as a frequency difference (using TE = 27 ms).

SNR efficiency, point spread broadening and distortion

The SNR efficiency of the 3D EPI protocol presented here (Table 1) resulted in a gain in SNR by a factor of 2 relative to the 3D GRE protocol. The relative SNR was calculated by $S = (1 - E_1)\ E_2 \sin\alpha\ /\ (1 - E_1\cos\alpha)$ (23) and the dependency of the SNR on voxel volume (Δxyz), number of samples acquired ($N_x N_y N_z$) and bandwidth (BW): $S\Delta xyz\ \sqrt{((N_x N_y N_z)/BW)}$, where $E_1 = \exp(-TR/T_1)$, $E_2 = \exp(-TE/T_2^*)$ and α is the flip angle.

The main reason why GRE imaging has a much lower SNR efficiency than EPI, is that GRE imaging performs data sampling only during a fraction of the 'lifetime of the signal', T_2^*, while EPI samples the signal over a much longer duration. The limiting factor for imaging speed with EPI is, therefore, the T_2^* of the tissue. We chose an EPI factor of 13, leading to an EPI train length of 23 ms, which is just below the T_2^* for most brain tissues. Long echo trains will reduce the efficiency of EPI, because in the extreme case, only noise is sampled, while shorter echo trains are still sub-optimal. There is a trade-off between EPI train length and image blurring or point spread widening, due to T_2^* decay during the readout. Using an EPI train length equal to the T_2^* of the imaged tissue, the broadening of the point spread function is less than 5% (24). For longer train lengths, or for tissues with shorter T_2^*, for example as may occur in regions with poor shimming such as above the nasal cavities

(Fig. 1), blurring can become noticeable.

The 3D GRE bandwidth could be reduced to such extent that the SNR efficiency of the 3D GRE protocol would become equal to that of the 3D EPI protocol (3). However, the total scan time for whole brain coverage would still be long, as the increased SNR efficiency obtained in this way cannot be traded off directly against imaging speed, as is the case for EPI.

The 3D EPI images showed only limited distortion, with a maximum observed distortion of 2.5 ± 0.5 mm for the lowest slice of the 3D GRE volume. This might be counter-intuitive, as EPI is well known to suffer from distortion. However, the amount of distortion depends strongly on the echo train length. With the echo train length used in this study, the BW in the phase encoding direction is 41 Hz, which corresponds to a displacement of 2.5 pixels (1.25 mm) per 100 Hz off-resonance. In our experience, using image based shimming at 7 T, the standard deviation of the off-resonance frequency distribution in the shimmed brain volume is around 60 Hz after shimming. In regions close to the nasal cavity and petrous bones, distortion will be strongest, and local gradients will lead to an apparently shorter T_2* and hence to noticeable blurring, which can be problematic for studies involving these regions.

The lower bandwidth for EPI sequences in the phase encoding direction results in larger water–fat shifts, which can be a disadvantage. However, because of the increased TR and the acquisition of multiple lines with each RF excitation, it is possible to include fat suppression or saturation slabs while still remaining within the SAR constraints, which are more easily reached at higher magnetic field strengths.

Implications

T_2*-weighted imaging provides valuable information in the study of both normal brain physiology and disease, as these images reflect brain tissue microstructure (4, 6, 25, 26). Neurodegenerative diseases in particular are associated with elevated iron depositions to which T_2*-weighted imaging is extremely sensitive (8–11). Unfortunately, patients with neurodegenerative diseases often have difficulties lying still for more than a few minutes, while T_2* weighted imaging is prone to motion artifacts (13). The proposed protocol is fast and will, hence, allow increased coverage in acceptable scanning time, or fast scanning of a limited brain area with lower chance of motion artifacts. Further reduction in scan time is expected from coils with more receive elements, which will allow for higher acceleration factors from parallel imaging. 3D EPI allows fast mapping of phase contrast and can hence con-

tribute to research on the origins of this contrast (27), as well as to accurate susceptibility mapping (20). 3D EPI using non-isotropic voxel sizes may prove beneficial for venography based on susceptibility-weighted imaging (28).

CONCLUSION

Fast T_2*-weighted anatomical imaging with high resolution and full brain coverage was obtained with 3D multi-shot EPI imaging. Spatial coverage and image signal to noise ratio is markedly improved compared to conventional 3D GRE imaging, given a fixed scan time and resolution, while image blurring and distortion are limited if the EPI train length remains short (not longer than the T_2* of the imaged tissue). 3D EPI provides steps (speed, whole brain coverage, and high isotropic resolution) that are necessary to utilize the benefits of high field MRI in research that employs T_2*-weighted imaging.

ACKNOWLEDGMENTS

The authors would like to thank F. Visser and Dr. J.J.M. Hoogduin for the constructive discussions on this topic.

REFERENCES

1. Li T-Q, van Gelderen P, Merkle H, Talagala L, Koretsky AP, Duyn J. Extensive heterogeneity in white matter intensity in high-resolution T2*-weighted MRI of the human brain at 7.0 T. NeuroImage 2006 ;32:1032–1040.
2. Cho Z-H, Min H-K, Oh S-H, Han J-Y, Park C-W, Chi J-G, Kim Y-B, Paek SH, Lozano AM, Lee KH. Direct visualization of deep brain stimulation targets in Parkinson disease with the use of 7-tesla magnetic resonance imaging. Journal of Neurosurgery 2010 ;113:639–647.
3. Duyn JH, van Gelderen P, Li T-Q, de Zwart JA, Koretsky AP, Fukunaga M. High-field MRI of brain cortical substructure based on signal phase. Proceedings of the National Academy of Sciences 2007 ;104:11796–11801.
4. Fukunaga M, Li T-Q, van Gelderen P, de Zwart JA, Shmueli K, Yao B, Lee J, Maric D, Aronova MA, Zhang G, Leapman RD, Schenck JF, Merkle H, Duyn JH. Layer-specific variation of iron content in cerebral cortex as a source of MRI contrast. Proceedings of the National Academy of Sciences 2010 ;107:3834 –3839.
5. Haacke EM, Cheng NYC, House MJ, Liu Q, Neelavalli J, Ogg RJ, Khan A, Ayaz M, Kirsch W, Obenaus A. Imaging iron stores in the brain using magnetic resonance imaging. Magnetic Resonance Imaging 2005 ;23:1–25.
6. He X, Yablonskiy DA. Biophysical mechanisms of phase contrast in gradient echo MRI. Proc Natl Acad Sci U S A 2009 ;106:13558–13563.
7. Zhong K, Leupold J, von Elverfeldt D, Speck O. The molecular basis for gray and white matter contrast in phase imaging. Neuroimage 2008 ;40:1561–6.
8. Bartzokis G, Cummings J, Perlman S, Hance DB, Mintz J. Increased Basal Ganglia Iron Levels in Huntington Disease. Arch Neurol 1999 ;56:569–574.
9. Mainero C, Benner T, Radding A, van der Kouwe A, Jensen R, Rosen BR, Kinkel RP. In vivo imaging of cortical pathology in multiple sclerosis using ultra-high field MRI. Neurology 2009 ;73:941–948.
10. Stankiewicz J, Panter SS, Neema M, Arora A, Batt CE, Bakshi R. Iron in chronic brain disorders: imaging and neurotherapeutic implications. Neurotherapeutics 2007 ;4:371–86.
11. van Rooden S, Maat-Schieman MLC, Nabuurs RJA, van der Weerd L, van Duijn S, van Duinen SG, Natté R, van Buchem MA, van der Grond J. Cerebral Amyloidosis: Postmortem Detection with Human 7.0-T MR Imaging System. Radiology 2009 ;253:788–796.
12. Haase A, Frahm J, Matthaei D, Hanicke W, Merboldt K-D. FLASH imaging. Rapid NMR imaging using low flip-angle pulses. Journal of Magnetic Resonance (1969) 1986 ;67:258–266.
13. Versluis MJ, Peeters JM, van Rooden S, van der Grond J, van Buchem MA, Webb AG, van Osch MJP. Origin and reduction of motion and f0 artifacts in high resolution T2*-weighted magnetic resonance imaging: Application in Alzheimer's disease patients. NeuroImage 2010 ;51:1082–1088.
14. Mansfield P, Maudsley AA, Bains T. Fast scan proton density imaging by NMR. Journal of Physics E: Scientific Instruments 1976 ;9:271.
15. Schär M, Kozerke S, Fischer SE, Boesiger P. Cardiac SSFP imaging at 3 Tesla. Magnetic Resonance in Medicine 2004 ;51:799–806.

16. Yarnykh VL. Actual flip-angle imaging in the pulsed steady state: A method for rapid three-dimensional mapping of the transmitted radiofrequency field. Magnetic Resonance in Medicine 2007 ;57:192–200.
17. Peters AM, Brookes MJ, Hoogenraad FG, Gowland PA, Francis ST, Morris PG, Bowtell R. T2* measurements in human brain at 1.5, 3 and 7 T. Magnetic Resonance Imaging 2007 ;25:748–753.
18. Rooney WD, Johnson G, Li X, Cohen ER, Kim S-G, Ugurbil K, Jr CSS. Magnetic field and tissue dependencies of human brain longitudinal H2O relaxation in vivo. Magnetic Resonance in Medicine 2007 ;57:308–318.
19. Conijn MMA, Geerlings MI, Luijten PR, Zwanenburg JJM, Visser F, Biessels GJ, Hendrikse J. Visualization of cerebral microbleeds with dual-echo T2*-weighted magnetic resonance imaging at 7.0 T. J. Magn. Reson. Imaging 2010 ;32:52–59.
20. Wharton S, Schäfer A, Bowtell R. Susceptibility mapping in the human brain using threshold-based k-space division. Magnetic Resonance in Medicine 2010 ;63:1292–1304.
21. Jenkinson M, Bannister P, Brady M, Smith S. Improved optimization for the robust and accurate linear registration and motion correction of brain images. Neuroimage 2002 ;17:825–841.
22. Poser BA, Koopmans PJ, Witzel T, Wald LL, Barth M. Three dimensional echo-planar imaging at 7 Tesla. NeuroImage 2010 ;51:261–266.
23. Ernst RR, Anderson WA. Application of Fourier transform spectroscopy to magnetic resonance. Review of Scientific Instruments 1966 ;37:93–102.
24. Haacke EM. The effects of finite sampling in spin-echo or field-echo magnetic resonance imaging. Magn Reson Med 1987 ;4:407–421.
25. Lee J, Shmueli K, Fukunaga M, van Gelderen P, Merkle H, Silva AC, Duyn JH. Sensitivity of MRI resonance frequency to the orientation of brain tissue microstructure. Proceedings of the National Academy of Sciences 2010 ;107:5130 –5135.
26. Reichenbach JR, Venkatesan R, Yablonskiy DA, Thompson MR, Lai S, Haacke EM. Theory and application of static field inhomogeneity effects in gradient-echo imaging. J Magn Reson Imaging 7:266–79.
27. Petridou N, Wharton SJ, Lotfipour A, Gowland P, Bowtell R. Investigating the effect of blood susceptibility on phase contrast in the human brain. NeuroImage 2010 ;50:491–498.
28. Haacke EM, Xu Y, Cheng Y-CN, Reichenbach JR. Susceptibility weighted imaging (SWI). Magnetic Resonance in Medicine 2004 ;52:612–618.